PAPER

Check for updates

Cobalt substitution slows forsterite carbonation in low-water supercritical carbon dioxide†

John S. Loring, ![ID] *[a] Tenley E. Webb, ![ID] [a] Mark E. Bowden, ![ID] [a]
Mark H. Engelhard ![ID] [b] and Sebastien N. Kerisit ![ID] *[a]

Cobalt recovery from low-grade mafic and ultramafic ores could be economically viable if combined with CO_2 storage under low-water conditions, but the impact of Co on metal silicate carbonation and the fate of Co during the carbonation reaction must be understood. In this study, *in situ* infrared spectroscopy was used to investigate the carbonation of Co-doped forsterite (($Mg,Co)_2SiO_4$) in thin water films in humidified supercritical CO_2 at 50 °C and 90 bar. Rates of carbonation of Co-doped forsterite to Co-rich magnesite (($Mg,Co)CO_3$) increased with water film thickness but were at least 10 times smaller than previously measured for pure forsterite at similar conditions. We suggest that the smaller rates are due to thermodynamic drivers that cause water films on Co-doped forsterite to be much less oversaturated with respect to Co-doped magnesite, compared to the pure minerals.

1. Introduction

Demand for cobalt has surged due to its increased use as cathode materials for rechargeable batteries and in superalloys for applications where high-temperature strength and wear/corrosion resistance are required.[1,2] Several of the world's largest economies have designated Co a critical element (CE) in part due to supply chain concerns related to majority foreign production.[3–6] Conventional high-grade magmatic sulfide and laterite ores of Co are becoming scarce,[3] requiring a search for alternate sources to maintain supply. Hence, there is growing urgency to develop methods to make the recovery of Co from lower-grade ores economically viable.[3,7]

Mafic and ultramafic rocks (*i.e.*, basalt and peridotite) contain low concentrations of Co (*e.g.*, up to 200 ppm on average in San Carlos olivine),[7] yet Co recovery from these low-grade ores could be made cost effective, given their high abundance and durable CO_2 storage potential. Carbonation could improve the economic viability of Co extraction from mafic or ultramafic rocks by both lowering processing costs and helping the mining industry reach net-zero CO_2 emissions.[8–14] Mafic and ultramafic rocks are comprised of silicate minerals rich in Ca^{2+}, Mg^{2+}, and Fe^{2+} cations that can react with CO_2 to form metal carbonates and amorphous silica.[15] CEs in silicate minerals

(*i.e.*, Co and Ni) have recently been proven recoverable through concurrent carbonation and sulfidization in bulk water with a CO_2 headspace.[16] However, carbonation for Co recovery under single-phase, humidified CO_2 has not yet been investigated. This low-water approach could reduce water usage, decrease waste, and favor the most thermodynamically stable carbonate products.[17,18]

In a humidified CO_2 environment, water adsorbs on metal silicate minerals as thin films that are only Å-to-nm in thickness, depending on the relatively humidity of the overlying gas/fluid.[17–20] Within these films, carbonic acid from the reaction of CO_2 and water dissolves the silicate minerals. Metal carbonate products nucleate and grow, resulting in permanent CO_2 capture. Thin water films demonstrate carbonation reactivity that is distinct from bulk water and could be exploited for more efficient Co recovery and durable CO_2 storage. Because of extraordinarily large mineral-surface-area-to-water-volume ratios, minor amounts of silicate dissolution can rapidly yield high degrees of carbonate supersaturation in thin water films.[18] The far-from-equilibrium conditions lead to faster carbonate growth at lower temperatures compared to bulk water.[18] Additionally, low water activity might avoid metastable hydrated Co carbonates by favoring the most thermodynamically stable carbonate products.[17]

The goal of this study was to understand the impact of Co on olivine (orthosilicate) carbonation and to determine the fate of Co during the carbonation reaction under low-water, humidified CO_2 conditions. Carbonation experiments were performed on a model synthetic nanometer-sized forsterite[21] (Mg_2SiO_4; the Mg-endmember of olivine) that contained 25 cation mole percent Co ($Mg_{1.5}Co_{0.5}SiO_4$, referred to hereafter as Co-doped

[a] Physical and Computational Sciences Directorate, Pacific Northwest National Laboratory, Richland, WA 99354, USA. E-mail: john.loring@pnnl.gov, sebastien.kerisit@pnnl.gov

[b] Energy and Environment Directorate, Pacific Northwest National Laboratory, Richland, WA 99354, USA

forsterite). Forsterite is a relatively reactive component of basalt with high CO_2 mineralization potential. While a concentration of 25% Co is orders of magnitude higher than Co concentrations in mafic and ultramafic rock samples,[22] it is a suitable amount for this study aimed at understanding and quantifying how Co affects forsterite carbonation rates. Carbonation reactions were carried out in H_2O-bearing supercritical (sc) CO_2 at 50 °C, 90 bar, and 72%, 85%, and 96% relative humidity (RH). We included 1% H_2 in the supercritical fluid to help prevent possible oxidation of Co(II) by water.

2. Experimental

2.1. Materials

Carbon dioxide and 1% hydrogen in carbon dioxide were purchased from Oxarc Inc. (99.999% purities). Reagent water was de-ionized (Barnstead NanoPure) and had a resistivity of 18.2 MΩ cm. Cobalt(II) chloride (anhydrous, 99.7% metals basis) was purchased from Thermo Scientific. Tetraethylorthosilicate (TEOS, ≥99.0%) and dodecylamine (98%) were purchased from Sigma-Aldrich. *tert*-Butylamine (99%) was purchased from Acros Organics. Magnesium methoxide (7–8% in methanol), methanol (anhydrous, 99.9%), and toluene (anhydrous, 99.8%) were purchased from Alfa Aesar.

2.2. Co-doped forsterite synthesis

The method of Anovitz *et al.*[23] for synthesizing pure nano-forsterite was modified to synthesize Co-doped forsterite. A stoichiometric mixture of magnesium methoxide, TEOS, and cobalt chloride was refluxed in a 2:1 toluene-to-methanol solvent for 24 hours. Dodecylamine was used as the surfactant to obtain nanoparticles, and *tert*-butylamine was added as a hydrolysis agent. Three 2-mL water aliquots were added 1, 10, and 20 hours after refluxing commenced, and an extra 1.75 g of *tert*-butylamine was added with the second water addition. A 2-L, 2-neck flask was used for the refluxing step, which was carried out in a nitrogen glovebox. The solution was cooled, removed from the glovebox, and the solvent was discarded by centrifuging and decanting. The gel was washed three times with a 2:1 toluene-to-methanol solvent and dried in air. This precursor material was gently ground in a mortar and pestle and then calcined at 900 °C (1 hour ramp, 45 minute soak) in a muffle furnace. Powder X-ray diffraction, X-ray photoelectron spectroscopic, and infrared (IR) spectroscopic characterization details of the calcined product are provided in the ESI† (Fig. S1, S2 and Table S1 respectively). Specific surface area was measured to be 20.1 $m^2 g^{-1}$ by the nitrogen Brunauer–Emmett–Teller (BET) method.

2.3. *In situ* high-pressure infrared spectroscopic titrations

In situ high-pressure IR titrations with water were carried out in $scCO_2$ or $scCO_2$ + 1% H_2 at 50 °C and 90 bar using an automated fluid-delivery apparatus coupled to a custom-built high-pressure IR reaction cell with both transmission and attenuated total reflection (ATR) IR optics. While a brief description is given in ESI,† complete details of the fluid delivery apparatus, reaction cell, spectrometer settings, spectral collection procedures, titration loop calibrations, and data analysis procedures have been described in detail elsewhere.[24,25]

Three types of IR experiments were performed and are summarized in Table S2 (ESI†): (1) calibrations (Cal_1 and Cal_2), (2) titrations (Ads_1 and Ads_2), and (3) time-dependent experiments (TDep_1, TDep_3, and TDep_3). The purpose of "calibrations" (Cal_1 and Cal_2) was to determine, using transmission IR, a correlation between the concentration and HOH-bend absorbance of dissolved water in the $scCO_2$, as well as to measure the concentration of water dissolved in the $scCO_2$ at saturation. After cell pressurization with $scCO_2$ or $scCO_2$ + 1% H_2, a transmission background spectrum was collected of the anhydrous fluid. Water was titrated stepwise into the pressurized cell every 60 minutes, and transmission IR spectra were collected of the wet $scCO_2$ at the end of this time period for each water addition. The transmission spectra were processed (see ESI†) in the HOH bending mode region of dissolved water to determine fluid RH. RH was calculated by dividing the absorbance of the HOH bend of water dissolved in the fluid by that same absorbance when the supercritical CO_2 fluid is saturated with water.

The purpose of "titrations" (Ads_1 and Ads_2) was to determine the amount of H_2O adsorbed on Co-doped forsterite as a function of RH. First, a massed (0.20 to 0.25 g) amount of Co-doped forsterite in a stainless-steel tray was inserted into the cell. The cell was then pressurized with $scCO_2$ or $scCO_2$ + 1% H_2, and a transmission background spectrum was collected of the anhydrous fluid. Water was titrated stepwise into the pressurized cell every 60 minutes, and transmission IR spectra were collected of the wet $scCO_2$ at the end of this time period for each water addition. Adsorbed H_2O concentrations in μmol m^{-2} were calculated from the difference between the known amount of H_2O added to the cell and the measured amount of water dissolved in the fluid; the mass of the forsterite; and its BET specific surface area. Water coverages in monolayers (ML) were calculated using molecular dynamics-derived parameters from Kerisit *et al.* for the (010) forsterite surface.[26,27] We estimate the uncertainty in the water coverage to be ± 0.1 mL based on the reproducibility of the IR titration experiments.

The purpose of "time-dependent experiments" was to monitor the carbonation of Co-doped forsterite as a function of time at a constant RH. First, an ATR-IR background spectrum was collected of the empty cell under vacuum (10^{-3} Torr). Then, 0.1 mL of a ~5 g L^{-1} of Co-doped forsterite suspension in isopropanol was evaporated onto the IRE to form an ATR overlayer. The cell was pressurized with anhydrous $scCO_2$, and a sample ATR IR spectrum of the Co-doped forsterite exposed to the anhydrous fluid and a background transmission spectrum of the anhydrous fluid were collected. Then, the cell was depressurized followed by insertion of a stainless-steel dish with 0.5 mL of 1.2 M, 2.2 M, or 2.7 M $CaCl_2$ ionic medium to maintain RH at 96%, 85%, or 72% for experiments TDep_1, TDep_3, or TDep_3, respectively. The cell was pressurized again, followed by ATR and transmission IR spectra collection

26466 | *Phys. Chem. Chem. Phys.*, 2024, **26**, 26465–26471

This journal is © the Owner Societies 2024

as a function of time for 120.4 hours to follow the carbonation of the Co-doped forsterite and monitor the RH.

2.4. Chemometrics analysis of ATR IR spectra

After pretreatment to correct for distortions inherent in ATR spectra and baseline drift spectra (see ESI† for more details), experiments TDep_1, TDep_3, or TDep_3 were normalized using the integrated absorbance under the SiO stretching bands of forsterite (770–1100 cm^{-1}) after exposure to anhydrous scCO$_2$ and before exposure to water. This normalization accounted for small differences in the amount of Co-doped forsterite deposited onto the IRE between experiments. Then, two-component multivariate curve resolution-alternating least squares (MCR-ALS)[28,29] chemometrics analyses were performed on the combined spectra from all three experiments from 1300–1700 cm^{-1}. Two eigenvectors from these analyses accounted for approximately 99.8% of the variance for all data sets, suggesting that the measured spectra could be reliably represented by two components. The first component, C1, was assigned to bicarbonate dissolved in water. The second component, C2, was assigned to Co-doped magnesite and adsorbed water by comparison to the spectrum of pure magnesite from the carbonation of pure forsterite.

3. Results and discussion

IR spectroscopic titrations were used to monitor the carbonation of Co-doped forsterite. In this technique, water is added to a pressurized cell equipped with both transmission and ATR IR optics. Transmission IR is used to measure the concentration of water dissolved in the supercritical fluid. ATR IR is used to measure the spectrum of the carbonating Co-doped forsterite, which is coated in a several-microns-thick layer on the ATR internal reflection element. Titration specifics are summarized in Table S2 (ESI†).

Calibrations Cal_1 and Cal_2 were control experiments of a vessel pressurized with scCO$_2$ and 1% H$_2$ in the absence of Co-doped forsterite. The purpose of the calibrations was to determine a correlation between the concentration and HOH-bend absorbance of dissolved water in the fluid and to measure the concentration of water in the fluid at saturation (Fig. S3A, ESI†). This concentration was 23.5 ± 0.4 mM, in reasonable agreement with a value of 24.6 ± 0.8 mM for pure scCO$_2$ at 50 °C and 90 bar that we reported previously.[19] Titrations Ads_1 and Ads_2 (Fig. S3B, ESI†) were similar to calibrations, but a known mass of Co-doped forsterite was included in the high-pressure cell. These experiments were carried out to measure the amount of H$_2$O adsorbed on Co-doped forsterite as a function of RH (Fig. S3B ESI†). Their purpose was also to determine a correlation between the integrated absorbance of the ATR IR OH stretching band of adsorbed water and the coverage of water in monolayers (MLs) calculated from transmission IR results (Fig. S3C, ESI†). Three time-dependent experiments were performed to follow the carbonation of Co-doped forsterite at fixed RH values for 5 days. An aqueous

solution of calcium chloride held in a stainless dish in the high-pressure cell was used to buffer the RH to 96%, 85%, and 72% RH in experiments TDep_1, TDep_2, and TDep_3, respectively. The linear regression in (Fig. S3C, ESI†) was used to extrapolate the coverage of adsorbed water from the integrated absorbance of the ATR IR OH stretching band of water after target RH values were achieved (typically about 2 hours). The water coverages for TDep_1, TDep_2, and TDep_3 were 16 ± 2, 5.4 ± 0.7, and 2.7 ± 0.5 mL, respectively.

Examples of IR spectra collected as a function of time during experiments TDep_1, TDep_2, and TDep_3 are shown in Fig. 1 in the CO stretching region of (bi)carbonate and the HOH bending region of water. The background spectrum was Co-doped forsterite exposed to 90 bar CO$_2$ + 1% H$_2$ at 0% RH for each experiment. The extent of reaction (EoR) for TDep_1 was estimated to be ~3 ± 1% based on the decrease in the SiO stretching bands of forsterite over the course of the experiment. EoR values for TDep_2 and TDep_3 were estimated to be ~2 ± 1% and ~1 ± 1%, respectively, based on the ratio of the absorbance of the CO stretching bands of the precipitated carbonate at the end of these experiments to that in experiment TDep_1.

A MCR-ALS analysis was carried out on the combined spectra from all three time-dependent experiments. Two components, C1 and C2 (Fig. 2(A)), modeled more than 99.8% of the variance in the IR data. Component C1 was assigned to bicarbonate and water based on a comparison with the spectrum of a MgHCO$_3$ solution in Fig. S4 (ESI†). Component C2 was assigned to Co-doped magnesite ((Mg,Co)CO$_3$) and water based on a comparison (Fig. 3) of the CO stretch at 1418 cm^{-1} of the carbonate that precipitated during experiment TDep_1 with the CO stretch at 1428 cm^{-1} of pure magnesite (MgCO$_3$) precipitated during the carbonation of pure forsterite.[19] The redshift of the CO stretch of the carbonate in component C2 is qualitatively consistent with a greater reduced mass due to Co substitution.

Quantifying metal substitution in carbonates is possible using vibrational spectroscopy,[30–32] and here we use the wavenumber position of the CO stretch of component C2 to place bounds on the Co concentration in the Co-doped magnesite. Based on the wavenumber positions of the CO stretch of pure magnesite (1436 cm^{-1}) *versus* sphaerocobaltite (CoCO$_3$, 1401 cm^{-1}) standards (Fig. S5, ESI†), and assuming that mole percent Co scales linearly with the wavenumber of the CO stretch, then we predict that the carbonate that precipitated in TDep_1 was doped in Co by ~50%. However, considering that the MgCO$_3$ formed during forsterite carbonation was redshifted by 8 cm^{-1} from the magnesite standard in Fig. S5 (ESI†), and assuming the same would be true for pure CoCO$_3$, then we calculate the carbonate that precipitated in TDep_1 was doped in Co by ~25%, which is in line with the mole percent Co of the forsterite. In sum, our IR analysis suggests that the Co concentration of the Co-doped magnesite is likely between ~25% and ~50%.

Bicarbonate concentrations increased rapidly in all three experiments within the first few hours of reaction (Fig. 2(B)). This fast rate could be due to the dissolution of a population of metals at high-energy sites on the Co-doped forsterite surface.
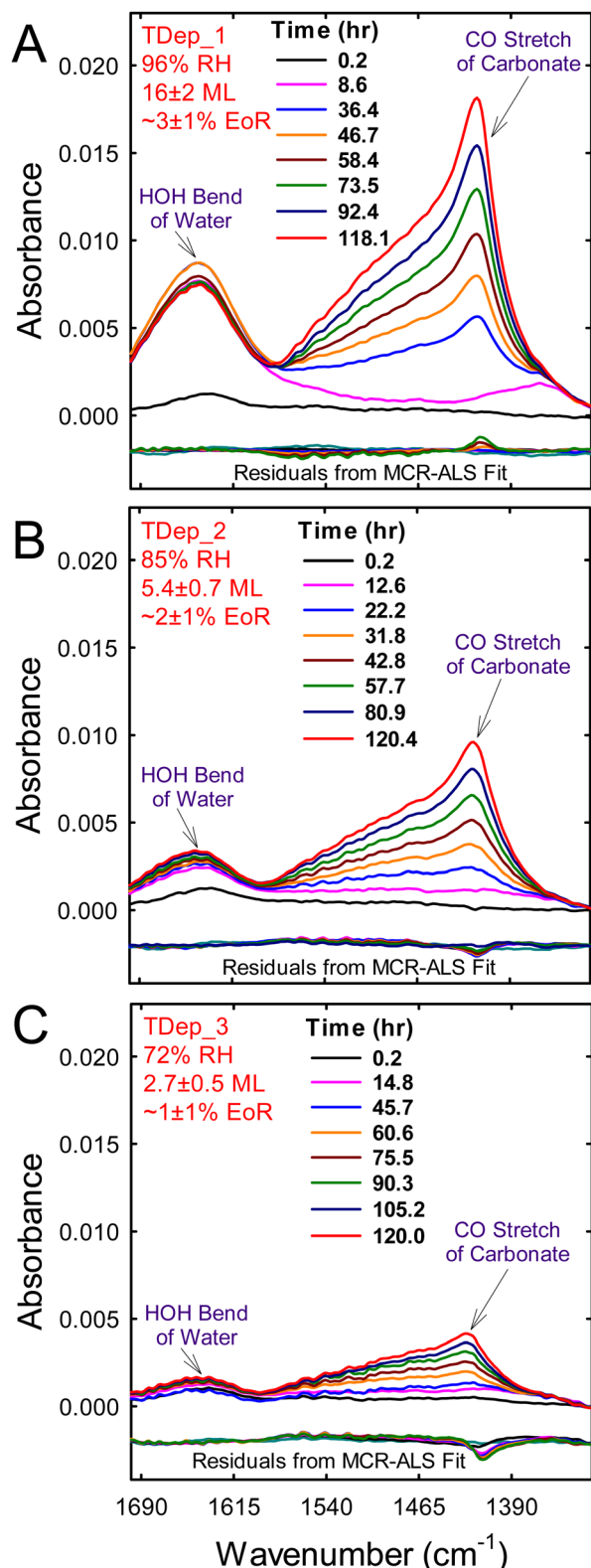
This journal is © the Owner Societies 2024

Phys. Chem. Chem. Phys., 2024, **26**, 26465–26471 | **26467**

Fig. 1 Select ATR IR spectra from experiments (A) TDep_1 at 96% RH, (B) TDep_2 at 85% RH and (C) TDep_3 at 72% RH, in which Co-doped forsterite was titrated with H_2O in $scCO_2$ + 1% H_2 at 50 °C and 90 bar. The background spectrum was unreacted Co-doped forsterite at pressure and temperature. The measured spectra from these data sets were combined and fit using a two-component MCR-ALS analysis; residuals are shown offset and below the measured spectra. EoR is an abbreviation for extent of reaction.
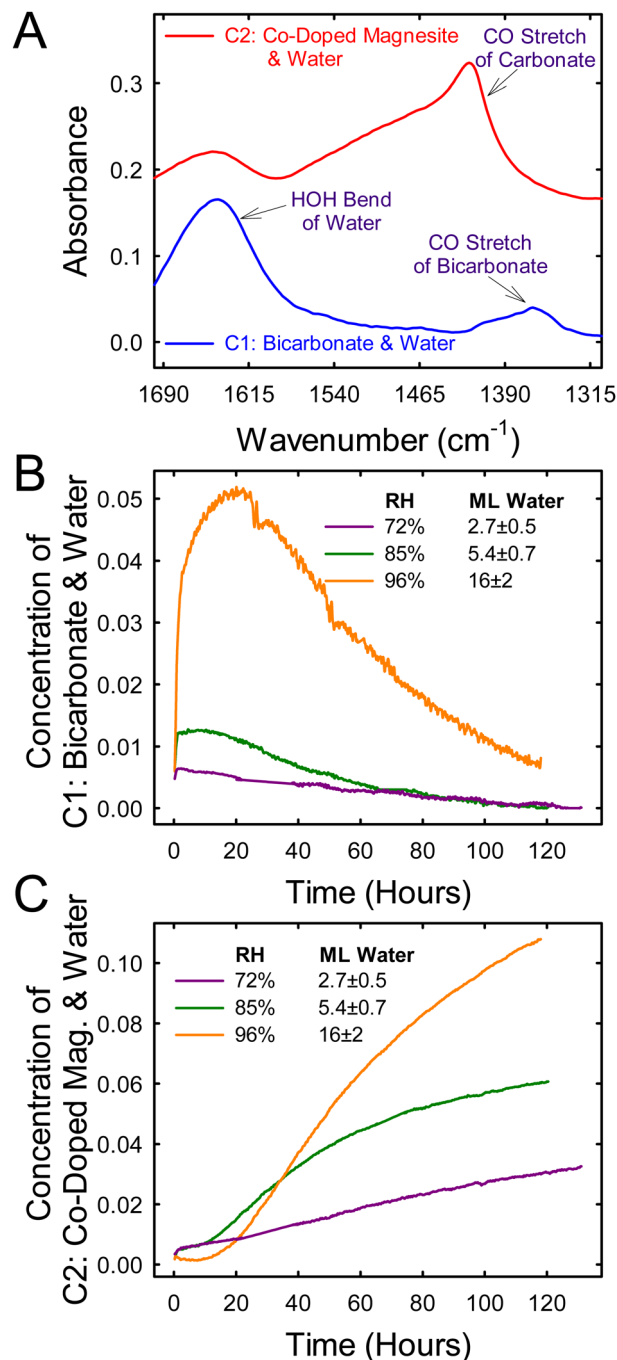

Fig. 2 Results from a two-component MCR-ALS analysis of the combined spectra from TDep_1 at 96% RH, TDep_2 at 85% RH, and TDep_3 at 72% RH. Components C1 and C2 are shown in (A) and are assigned to bicarbonate and Co-doped magnesite, respectively. Water is also present in both components. The concentrations of C1 and C2 are shown in (B) and (C), respectively, for each experiment.

After Co-doped magnesite nucleated and began to grow, bicarbonate concentrations decreased. This is likely because the dissolved metal and bicarbonate concentrations are decreasing towards the solubility of the carbonate.

Co-doped magnesite had already nucleated in the beginning of experiments TDep_2 and TDep_3, but it took about 10 hours
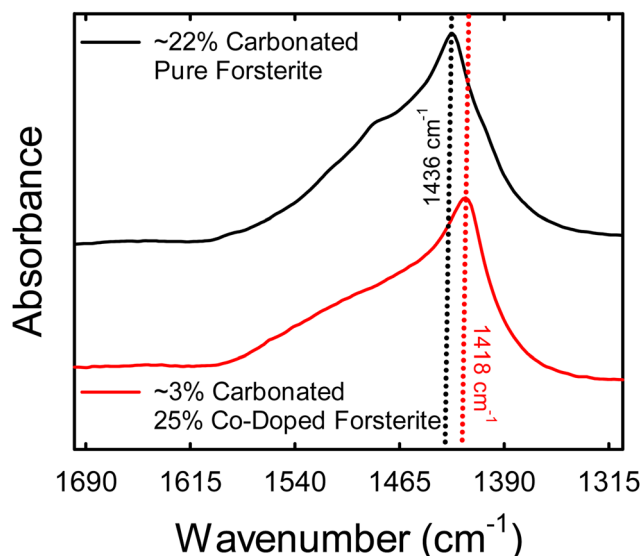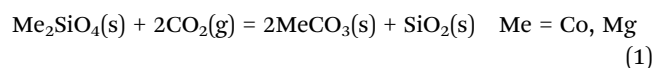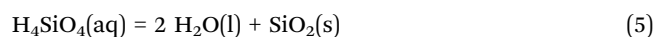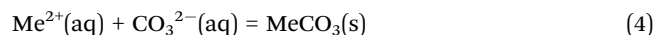
26468 | *Phys. Chem. Chem. Phys.*, 2024, **26**, 26465–26471

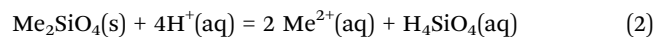This journal is © the Owner Societies 2024

Fig. 3 (Top, black) The spectrum of the carbonate precipitated during the carbonation of pure forsterite after depressurizing the IR cell and pulling a vacuum. This carbonate was confirmed to be predominately magnesite (MgCO₃) by X-ray diffraction.[19] (Bottom, red) The spectrum of the metal carbonate that precipitated during the carbonation of 25% Co-doped forsterite in experiment TDep_1 after depressurizing the IR cell and pulling a vacuum. We assign this spectrum to be Co-doped magnesite ((Mg,Co)CO₃) based on its similarity with that of magnesite.

to nucleate in TDep_1 with the thickest water film (Fig. 2(C)). Rates of Co-doped magnesite growth slowed with increasing reaction time in TDep_1 and TDep_2. This is consistent with a decrease in the extent of supersaturation with respect to the carbonate as the bicarbonate concentration decreased and the population of metals at high-energy surface sites were fully consumed. The rate of Co-doped magnesite formation was slowest for TDep_3, but it was relatively constant over the 5-day reaction time. TDep_3 had the thinnest water film of the three experiments, and thus the steady growth of carbonate could be because diffusive ion transport became limiting.[20]

Rates and extents of carbonation are significantly smaller for Co-doped forsterite than for pure forsterite under similar humidified scCO₂ conditions. For example, Fig. S6 (ESI†) compares spectra from experiment TDep_2 carried out at 85% RH with previously reported spectra from a similar experiment for pure forsterite carbonated at 83% RH.[19] The EoR of the experiment with pure forsterite after 5 days was ~22 ± 2% versus ~2 ± 1% for Co-doped forsterite. Thus, we estimate that the carbonation rate of Co-doped forsterite is at least 10 times smaller than for pure forsterite. This difference can be rationalized by considering the extents to which the water films are likely supersaturated with respect to carbonate phases, which can be understood in terms of the bulk aqueous equilibrium constants for olivine dissolution and respective carbonate formation. The carbonation of an olivine endmember can be written

$$Me_2SiO_4(s) + 2CO_2(g) = 2MeCO_3(s) + SiO_2(s) \quad Me = Co, Mg \quad (1)$$

and is the sum of the following reactions:

$$Me_2SiO_4(s) + 4H^+(aq) = 2\ Me^{2+}(aq) + H_4SiO_4(aq) \quad (2)$$

$$H_2O(l) + CO_2(g) = 2\ H^+(aq) + CO_3^{2-}(aq) \quad (3)$$

$$Me^{2+}(aq) + CO_3^{2-}(aq) = MeCO_3(s) \quad (4)$$

$$H_4SiO_4(aq) = 2\ H_2O(l) + SiO_2(s) \quad (5)$$

In bulk solution at 50 °C, $\log K_{eq}$ for the dissolution reaction (2) is 2.67 for Me = Co versus 22.49 for Me = Mg,[33] yet, for the carbonate formation reaction (4), $\log K_{eq}$ is −10.15 for Me = Co (sphaerocobaltite)[34] versus −7.99 for Me = Mg (magnesite).[35] In other words, Co_2SiO_4 is 19.8 orders of magnitude less soluble than Mg_2SiO_4, but $CoCO_3$ is only 2.2 orders of magnitude less soluble than $MgCO_3$. Thus, even though the forward dissolution rate of Co_2SiO_4 is approximately one order of magnitude higher than that of Mg_2SiO_4,[36] the water film is expected to approach equilibrium with respect to Co_2SiO_4 much more rapidly than with respect to Mg_2SiO_4, which, in turn, slows down the dissolution reaction of Co_2SiO_4 to a greater extent due to the much-reduced chemical affinity. Hence, for a given carbonate activity, water films on Mg_2SiO_4 are expected to be much more concentrated in divalent cations than water films on Co_2SiO_4 and, as a result, to be significantly more over-saturated with respect to $MgCO_3$ versus water films on Co_2SiO_4 with respect to $CoCO_3$. This difference should translate to lower rates of $CoCO_3$ formation during Co_2SiO_4 carbonation than rates of $MgCO_3$ formation for Mg_2SiO_4 carbonation. We suggest that the $\log K_{eq}$ values for the silicate dissolution and carbonate formation (reactions (2) and (4), respectively) of the mixed Mg–Co olivines scale with those values of the endmembers.[37] Accordingly, the extents to which the water films become supersaturated with respect to carbonate products in the mixed Mg–Co olivine systems should lead to rates of carbonation that are between those of the endmembers. Hence, the impact of the solubility of the mixed Mg–Co olivine on the extent of saturation of the water films with respect to carbonate products is likely the reason that carbonation rates and EoRs are much smaller for Co-doped forsterite versus pure forsterite.

4. Conclusion

This study furthers our understanding of the impact of Co and its fate during olivine carbonation in low-water conditions. Co substitution lowers olivine solubilities, extents of saturation with respect to carbonate products, and thus carbonation rates. Co-doped magnesite is the predominant product in thin water films in contrast to bulk aqueous conditions, where metastable intermediates such as hydroxides and hydrous carbonates form much faster and are kinetically stable.[17,34] We hypothesize that at the low Co concentrations relevant to natural olivine samples,[7] the effect of Co on carbonation rates will be much reduced. We will test this hypothesis in future studies that will investigate carbonation of olivines containing a range of Co concentrations. Sulfide reactants will be included to track the partitioning of Co into sulfide minerals during carbonation.[16]

This journal is © the Owner Societies 2024

Phys. Chem. Chem. Phys., 2024, **26**, 26465–26471 | **26469**

Author contributions

J. S. L. conceived, designed, and performed the research, analysed data, and wrote the article. T. E. W., M. E. B., and M. H. E. performed the research and analysed data. S. N. K. and T. E. W. also analysed data and wrote the article.

Data availability

Infrared spectroscopic details, X-ray diffraction methods, X-ray photoelectron spectroscopic methods, Tables S1, S2, and Fig. S1–S6 are available in the ESI.†

Conflicts of interest

There are no conflicts to declare.

Acknowledgements

References

1 T. E. Graedel and A. Miatto, *Resour., Conserv. Recycl.*, 2022, **184**, 106441.

2 F. Crundwell, M. Moats and V. Ramachandran, *Extractive Metallurgy of Nickel, Cobalt and Platinum Group Metals*, Elsevier, Oxford, 2011.

3 J. F. Slack, B. E. Kimball and K. B. Shedd, Cobalt, Report 1411339916, US Geological Survey, 2017.

4 U.S. Geological Survey and Department of the Interior, Federal Register, 2022, 87, 10381-10382.

5 U.S. Geological Survey, Mineral commodity summaries 2023, Reston, VA, 2023.

6 X. Fu, D. N. Beatty, G. G. Gaustad, G. Ceder, R. Roth, R. E. Kirchain, M. Bustamante, C. Babbitt and E. A. Olivetti, *Environ. Sci. Technol.*, 2020, **54**, 2985–2993.

7 Q. Dehaine, L. T. Tijsseling, H. J. Glass, T. Törmänen and A. R. Butcher, *Miner. Eng.*, 2021, **160**, 106656.

8 F. Wang, D. Dreisinger, M. Jarvis, T. Hitchins and L. Trytten, *Chem. Eng. J.*, 2021, **406**, 126761.

9 J. Hamilton, S. Wilson, B. Morgan, A. Harrison, C. Turvey, D. Paterson, G. Dipple and G. Southam, *Econ. Geol.*, 2020, **115**, 303–323.

10 F. Wang and D. Dreisinger, *Sep. Purif. Technol.*, 2023, **321**, 124268.

11 C. Matus, S. Stopic, S. Etzold, D. Kremer, H. Wotruba, C. Dertmann, R. Telle, B. Friedrich and P. Knops, *Metals*, 2020, **10**, 811.

12 S. Wilson and J. Hamilton, *Proc. Natl. Acad. Sci. U. S. A.*, 2022, **119**, e2212424119.

13 S. Khan, M. Shoaib, L. K. Fiddes, O. B. Wani and E. R. Bobicki, *Green Chem.*, 2024, **26**, 1289–1296.

14 R. M. Santos, A. Van Audenaerde, Y. W. Chiang, R. I. Iacobescu, P. Knops and T. Van Gerven, *Metals*, 2015, **5**, 1620–1644.

15 S. Ó. Snæbjörnsdóttir, B. Sigfússon, C. Marieni, D. Goldberg, S. R. Gislason and E. H. Oelkers, *Nat. Rev. Earth Environ.*, 2020, **1**, 90–102.

16 F. Wang and D. Dreisinger, *Proc. Natl. Acad. Sci. U. S. A.*, 2022, **119**, e2203937119.

17 S. T. Mergelsberg, S. N. Kerisit, E. S. Ilton, O. Qafoku, C. J. Thompson and J. S. Loring, *Chem. Commun.*, 2020, **56**, 12154–12157.

18 S. N. Kerisit, S. T. Mergelsberg, C. J. Thompson, S. K. White and J. S. Loring, *Environ. Sci. Technol.*, 2021, **55**, 12539–12548.

19 S. T. Mergelsberg, B. P. Rajan, B. A. Legg, L. Kovarik, S. D. Burton, G. M. Bowers, M. E. Bowden, O. Qafoku, C. J. Thompson and S. N. Kerisit, *et al.*, *Environ. Sci. Technol. Lett.*, 2023, **10**, 98–104.

20 E. Placencia-Gómez, S. N. Kerisit, H. S. Mehta, O. Qafoku, C. J. Thompson, T. R. Graham, E. S. Ilton and J. S. Loring, *Environ. Sci. Technol.*, 2020, **54**, 6888–6899.

21 L. M. Anovitz, A. J. Rondinone, L. Sochalski-Kolbus, J. Rosenqvist and M. C. Cheshire, *J. Colloid Interface Sci.*, 2017, **495**, 94–101.

22 S. Lambart, S. Hamilton and O. I. Lang, *Chem. Geol.*, 2022, **605**, 120968.

23 L. M. Anovitz, A. J. Rondinone, L. Sochalski-Kolbus, J. Rosenqvist and M. C. Cheshire, *J. Colloid Interface Sci.*, 2017, **495**, 94–101.

24 C. J. Thompson, P. F. Martin, J. Chen, P. Benezeth, H. T. Schaef, K. M. Rosso, A. R. Felmy and J. S. Loring, *Rev. Sci. Instrum.*, 2014, **85**, 044102.

25 J. S. Loring, D. H. Bacon, R. D. Springer, A. Anderko, S. Gopinath, C. M. Yonkofski, C. J. Thompson, B. P. McGrail, K. M. Rosso and H. T. Schaef, *J. Chem. Eng. Data*, 2017, **62**, 1608–1614.

26 S. Kerisit, E. J. Bylaska and A. R. Felmy, *Chem. Geol.*, 2013, **359**, 81–89.

27 S. Kerisit, J. H. Weare and A. R. Felmy, *Geochim. Cosmochim. Acta*, 2012, **84**, 137–151.

26470 | *Phys. Chem. Chem. Phys.*, 2024, **26**, 26465–26471

This journal is © the Owner Societies 2024

28 A. Gorzsás, *Open source MATLAB script from the Vibrational Spectroscopy Core Facility*, Umeå University, Umeå Sweden, 2017.

29 A. de Juan and R. Tauler, *Crit. Rev. Anal. Chem.*, 2006, **36**, 163–176.

30 L. Borromeo, U. Zimmermann, S. Andò, G. Coletti, D. Bersani, D. Basso, P. Gentile, B. Schulz and E. Garzanti, *J. Raman Spectrosc.*, 2017, **48**, 983–992.

31 N. Rividi, M. van Zuilen, P. Philippot, B. Ménez, G. Godard and E. Poidatz, *Astrobiology*, 2010, **10**, 293–309.

32 Y. Kim, M.-C. Caumon, O. Barres, A. Sall and J. Cauzid, *Spectrochim. Acta, Part A*, 2021, **261**, 119980.

33 J. Johnson, F. Anderson and D. L. Parkhurst, *Database thermo.com.V8.R6.230, rev. 1.11*, Laboratory, L.L.N. (Editor), Livermore, CA., 2000.

34 S. L. Riechers, E. S. Ilton, O. Qafoku, Y. Du and S. N. Kerisit, *Chem. Geol.*, 2022, **605**, 120951.

35 P. Benezeth, G. D. Saldi, J. L. Dandurand and J. Schott, *Chem. Geol.*, 2011, **286**, 21–31.

36 H. R. Westrich, R. T. Cygan, W. H. Casey, C. Zemitis and G. W. Arnold, *Am. J. Sci.*, 1993, **293**, 869–893.

37 I. F. Barton, H. Yang and M. D. Barton, *Can. Mineral.*, 2014, **52**, 653–670.

This journal is © the Owner Societies 2024

Phys. Chem. Chem. Phys., 2024, **26**, 26465–26471 | **26471**